Simulation of droplet breakage in turbulent liquid-liquid dispersions with CFD-PBM: Comparison of breakage kernels

Simulation of droplet breakage in turbulent liquid-liquid dispersions with CFD-PBM: Comparison of breakage kernels / Gao, Zhengming; Li, Dongyue; Buffo, Antonio; Podgórska, Wioletta; Marchisio, Daniele. - In: CHEMICAL ENGINEERING SCIENCE. - ISSN 0009-2509. - 142:(2016), pp. 277-288. [10.1016/j.ces.2015.11.040]

Publisher:
Elsevier Ltd

Published
DOI:10.1016/j.ces.2015.11.040

Simulation of droplet breakage in turbulent liquid-liquid dispersions with CFD-PBM: comparison of breakage kernels

Zhengming Gao[a], Dongyue Li[a], Antonio Buffo[b], Wioletta Podgórska[c], Daniele L. Marchisio[d,*]

[a]State Key Laboratory of Chemical Resource Engineering, School of Chemical Engineering, Beijing University of Chemical Technology, Beijing, China
[b]Aalto University, Department of Biotechnology and Chemical Technology, Espoo, Finland
[c]Faculty of Chemical and Process Engineering, Warsaw University of Technology, Warsaw, Poland
[d]Institute of Chemical Engineering, Department of Applied Science and Technology, Politecnico di Torino, Torino, Italy

---

Abstract

In this work droplet breakage in turbulent liquid-liquid dispersions is simulated by using computational fluid dynamics and population balance modelling. Model predictions are validated against experimental data for eight test cases, namely stirred tanks with different geometries and different continuous and disperse phases. The two first test cases correspond to two geometrically similar stirred tanks (one being the scale up of the other) working under the same power input per unit mass with water as continuous phase and a mixture of chlorobenzene and toluene as disperse phase. The last six test cases correspond to a slightly different geometry, working with water as continuous phase and different silicon oils as disperse phase, characterized by different viscosity values, stirred at different stirring rates. Simulations are performed with our implementation of the quadrature method of moments for the solution of the population balance model into the open-source computational fluid dynamics code OpenFOAM. Two different breakage kernels are considered in this work, based respectively on the classical homogeneous

---

[*] Corresponding author: Daniele Marchisio; e-mail: daniele.marchisio@polito.it; tel.: +390110904622; fax: +390110904699

and multifractal turbulence theories. Analysis of the kernels and comparison with experiments reveal that the second kernel results is better agreement with experiments, a more accurate description of the underlying physics and presents the additional advantage of having no fitting constants.

Keywords:
Stirred tanks, Liquid-liquid dispersions, Computational fluid dynamics, Population balance model, quadrature method of moments, breakage

---

1. Introduction

Liquid-liquid turbulent dispersions are omnipresent in the chemical industry for conducting several operations (i.e. extraction, polymerization, emulsification, etc.) with important implications in the food, cosmetic, mineral and petro-chemical fields. Numerous properties of the dispersion are of interest, but one of the most important is the droplet size distribution (DSD), which determines its stability, rheological features and its capability of exchanging mass (and energy and momentum) with the continuous phase. Knowledge of the DSD and its relationship with the fluid dynamics of the above mentioned apparatuses is also very important, as shown by Maaß et al. (2011); Lane et al. (2005); Drumm et al. (2009).

This knowledge can be achieved nowadays with computational fluid dynamics (CFD) coupled with a Population Balance Model (PBM). Among the different methods available, the one most interesting for the investigation of industrial scale liquid-liquid multiphase systems, is the two-fluid model (TFM) (Drew, 1982; Drew and Passman, 2006), implicitly assuming that one of the two phases is continuous, whereas the other one is disperse. The TFM is coupled with PBM to predict the evolution of the DSD (Ramkrishna, 2000), as shown in numerous applications (Hu et al., 2015; Attarakih et al., 2015; Favero et al., 2015). Many methods have been developed to solve the PBM, such as the classes method (CM) (Kumar and Ramkrishna, 1996), the Monte Carlo method (MCM)(Lin et al., 2002; Buffo et al., 2013b; Zhang and You, 2015; Hussain et al., 2015) and the method of moments (MOM) (Hulbert and Katz, 1964). To overcome the so-called closure problem in the MOM, a strategy based on the use of a quadrature approximation was introduced, resulting in the quadrature method of moment (QMOM) (McGraw, 1997), the Direct Quadrature Method of Moments (DQMOM) (Marchisio and Fox, 2005), the Conditional Quadrature Method of Moments (CQMOM) (Cheng et al., 2010; Yuan and Fox, 2011) and the Sectional Quadrature Method of Moments (SQMOM) (Attarakih et al., 2009). An overview of these methods can be found in the literature (Marchisio and Fox, 2013).

One major problem in the development of a fully-predictive model is the availability of reliable sub-models for describing the different phenomena involved, notably the kernels for coalescence and breakage. These kernels should be derived from theory and contain universal constants, that need not to be tuned or fitted to match experimentally observed trends. One of the first investigations in this field was carried out by Coulaloglou and Tavlarides (1977), that together with Ramkrishna (1974) showed how to use the statistical theory of turbulence to derive kernels. The same methodology was then applied by Luo and Svendsen (1996) to simulate gas-liquid systems. In more recent years other studies have appeared and new kernels proposed (Martínez-Bazán et al., 1999; Alopaeus et al., 2002). Although some of these kernels resulted in decent agreement with experiments, the constants appearing in them seem not to be universal. Moreover, these kernels often fail when challenged to simulate the scale-up or scale-down of an apparatus or when the physical properties of the continuous or disperse phases are changed. Experiments conducted at different scales showed that some important phenomena (due to turbulence intermittency) are generally neglected in most of the kernels available in the literature (Podgórska, 2005). Also experiments conducted at high viscosity ratios (between disperse and continuous phases) showed non-trivial effects that are often not captured by the currently available kernels (Cho and Kamal, 2002; Becker et al., 2014).

This work focuses on one particular mechanism of droplet breakage and aims at comparing the predictions obtained with our recent implementation of QMOM in OpenFOAM (Buffo et al., 2013a) by testing two different breakage kernels. The kernels tested are the one by Coulaloglou and Tavlarides (1977) (CT), based on the Kolmogorov turbulence theory, and the “multifractal” (MF) kernel, based on the multifractal theory of turbulence, developed by Baldyga and Podgórska (1998). The adoption of this latter kernel, together with the use of OpenFOAM are the main novelties of this work. Simulation predictions are compared with experiments corresponding to eight different test cases, allowing to draw some general conclusions. The two first test cases correspond to two geometrically similar stirred tanks (one being the scale-up of the other) working under the same power input per unit mass, with water as continuous phase and a mixture of chlorobenzene and toluene as disperse phase (Podgórska, 2006a). The last six test cases correspond to a same geometry, working under different stirring rates, with water as continuous phase and three different silicon oils, characterized by different viscosity values, as disperse phases (Podgórska, 2006b).

2. Governing equations

The main equations employed in the TFM and in the PBM will be discussed here, together with the description of the constitutive equations for the MF and for the CT breakage kernels.

2.1. Two-fluid model

As already mentioned, in the TFM both phases are described in terms of their volume fractions and average velocities and treated as continuum inter-penetrating phases. The continuity equation for the volume fraction of the disperse phase reads as follows:

$$\frac{\partial\left(\alpha_{\mathrm{d}}\rho_{\mathrm{d}}\right)}{\partial t}+\nabla\cdot\left(\alpha_{\mathrm{d}}\rho_{\mathrm{d}}\mathbf{U}_{\mathrm{d}}\right)=0, \tag{1}$$

where α_{d} is the volume fraction of the disperse phase, ρ_{d} is its density and $\mathbf{U}_{\mathrm{d}}$ is its average velocity. The volume fraction of the continuous phase (α_{c}) is generally calculated by knowing that volume fractions sum to unity ($\alpha_{\mathrm{d}}+\alpha_{\mathrm{c}}=1$).

The average velocities of the disperse phase ($\mathbf{U}_{\mathrm{d}}$) and of the continuous phase ($\mathbf{U}_{\mathrm{c}}$) are calculated by solving the corresponding momentum balance equations:

$$\begin{split}\frac{\partial\left(\alpha_{\mathrm{d}}\rho_{\mathrm{d}}\mathbf{U}_{\mathrm{d}}\right)}{\partial t}+\nabla\cdot\left(\alpha_{\mathrm{d}}\rho_{\mathrm{d}}\left(\mathbf{U}_{\mathrm{d}}\otimes\mathbf{U}_{\mathrm{d}}\right)\right)+\\ \nabla\cdot\left(\alpha_{\mathrm{d}}\boldsymbol{\tau}_{\mathrm{d}}\right)+\nabla\cdot\left(\alpha_{\mathrm{d}}\mathbf{R}_{\mathrm{d}}\right)=-\alpha_{\mathrm{d}}\nabla p+\alpha_{\mathrm{d}}\rho_{\mathrm{d}}\mathbf{g}+\mathbf{M}_{\mathrm{d}},\end{split} \tag{2}$$

$$\begin{split}\frac{\partial\left(\alpha_{\mathrm{c}}\rho_{\mathrm{c}}\mathbf{U}_{\mathrm{c}}\right)}{\partial t}+\nabla\cdot\left(\alpha_{\mathrm{c}}\rho_{\mathrm{c}}\left(\mathbf{U}_{\mathrm{c}}\otimes\mathbf{U}_{\mathrm{c}}\right)\right)+\\ \nabla\cdot\left(\alpha_{\mathrm{c}}\boldsymbol{\tau}_{\mathrm{c}}\right)+\nabla\cdot\left(\alpha_{\mathrm{c}}\mathbf{R}_{\mathrm{c}}\right)=-\alpha_{\mathrm{c}}\nabla p+\alpha_{\mathrm{c}}\rho_{\mathrm{c}}\mathbf{g}-\mathbf{M}_{\mathrm{d}},\end{split} \tag{3}$$

where p is the pressure shared by the two phases (Drew, 1982; Drew and Passman, 2006), $\boldsymbol{\tau}_{\mathrm{d}}$ and $\boldsymbol{\tau}_{\mathrm{c}}$ are the viscous-stress tensors, $\mathbf{R}_{\mathrm{d}}$ and $\mathbf{R}_{\mathrm{c}}$ are the Reynolds-stress tensors, $\mathbf{g}$ is the gravitational acceleration vector and $\mathbf{M}_{\mathrm{d}}$ is the interfacial force term. The viscous-stress and Reynolds-stress tensors for the disperse phase (and similarly for the continuous phase) can be modeled by using the well-known Boussinesq approximation.

The Reynolds-averaged Navier-Stokes equation (RANS) approach was found to be a good trade-off between accuracy and computational costs for fluid-fluid systems (Petitti et al., 2009, 2013). In particular the extension to multi-phase systems of the single-phase standard $k-\varepsilon$ model is the most popular method to simulate dilute turbulent multi-phase flows (Gosman et al., 1992; Behzadi et al., 2004) and is also adopted in this work.

The right-hand sides of Eq. (2) and of Eq. (3) contains some important terms that deserve a thorough discussion. $\mathbf{M}_{\mathrm{d}}$ describes the momentum exchange between the two phases and requires a certain degree of modelling. This term is usually composed by three phase-weighted forces: drag, virtual mass and lift (Gosman et al., 1992). In the present work, only the drag force is taken into account, whereas the others are neglected; this simplification hypothesis is indeed valid for liquid-liquid dispersions in stirred tanks, as the velocity field is dominated by the turbine rotation. The drag force can be calculated with the following equation (Rusche, 2003):

$$\mathbf{M}_{\mathrm{d}} = \alpha_{\mathrm{d}}\alpha_{\mathrm{c}}\left(\frac{3}{4}C_{\mathrm{D}}\frac{\rho_{\mathrm{d}}}{d}\left|\mathbf{U}_{\mathrm{r}}\right|\right)\mathbf{U}_{\mathrm{r}}, \tag{4}$$

where $\mathbf{U}_{\mathrm{r}} = \mathbf{U}_{\mathrm{c}} - \mathbf{U}_{\mathrm{d}}$ is the relative slip velocity and C_{D} is the drag coefficient, which is usually determined empirically and depends on the properties of the droplets. In this work, the correlation of Schiller and Naumann (1935) is used:

$$C_{\mathrm{D}} = \begin{cases} \frac{24}{\mathrm{Re}}\left(1 + 0.15\mathrm{Re}^{0.687}\right) & \mathrm{Re} \leq 1000 \\ 0.44 & \mathrm{Re} > 1000 \end{cases}, \tag{5}$$

where the droplet Reynolds number is based on the local droplet diameter: $\mathrm{Re} = \frac{\rho_{\mathrm{c}}|\mathbf{U}_{\mathrm{r}}|d}{\mu_{\mathrm{c}}}$. This correlation was found to be adequate for dilute systems, characterized in other words by low volume fractions of the disperse phase (i.e. smaller than 1 %). Moreover, it is worth mentioning that this correlation does not consider the role of the turbulence on the drag force (Karimi et al., 2012).

It is worth mentioning here that the droplet diameter appears in Eq. (5), implying that the drag force acting on each droplet is different for polydisperse systems. A common approximation is to calculate the average drag force acting on a population of droplets by using the mean Sauter diameter, i.e. $d \approx d_{32}$ (Buffo and Marchisio, 2014). This approximation was found to be valid for most liquid-liquid dispersion, where the DSD is often quite narrow, the densities of the disperse and continuous phases are close to each other and when the DSD is limited in the micrometer range. As well known the mean Sauter diameter is the ratio between the moments of order three and two of the DSD, therefore the problem is now how to calculate the moments of the DSD.

2.2. Population Balance Model

The droplet size distribution (DSD) changes due to breakage and coalescence and its evolution is dictated by the PBM. Due to the low volume fraction of the disperse phase, coalescence is neglected in this work, and only breakage is considered, as done in other similar works (Gäbler et al., 2006; Maaß et al., 2012). The main equation constituting the PBM that governs the evolution of the DSD reads as follows (omitting space and time dependencies):

$$\frac{\partial n(d)}{\partial t} + \nabla \cdot (n(d)\mathbf{U}_{\mathrm{d}}) = \int\limits_{d}^{\infty} \beta\,(d, d')g\,(d')\,n\,(d')\;\mathrm{d}d' - g\,(d)\,n\,(d)\,, \qquad (6)$$

where $n(d)$ is the DSD and d is the droplet size, g is the breakage kernel (or frequency of breakage) and $\beta(d, d')$ is the daughter distribution function stating the size distribution of daughter droplets originating from a mother droplet of size d'. More details about Eq. (6) can be found in the book of Ramkrishna (2000); McGrady and Ziff (1987) proposed the adopted formulation for breakage. A detailed derivation of Eq. (6) when written by using length as internal coordinate can be found in the literature (see for example Marchisio et al. (2003)).

As mentioned QMOM is used to solve the PBM. The method is based on the idea of solving transport equations for the moments of the DSD. As already mentioned the lower-order moments are very important since they are related to specific physical properties of the DSD, most importantly the mean Sauter diameter is defined as follows: $d_{32} = \frac{m_3}{m_2}$. The resulting closure problem emerging on the right-hand side of Eq. (6) is overcome by using a quadrature approximation of order N, resulting in the following "representation" of the moment of order k:

$$m_k(t,\mathbf{x}) = \int_0^{+\infty} n\left(t,\mathbf{x},d\right) d^k \,\mathrm{d}d \approx \sum_{\alpha=1}^{N} w_\alpha d_\alpha^k, \tag{7}$$

where d_α are the N abscissas and w_α are the N weights, in turn calculated from the first $2N$ lower-order moments with the product-difference or the Wheeler algorithms, as illustrated in the book by Marchisio and Fox (2013).

By applying QMOM the transport equation for the moment of order k becomes:

$$\frac{\partial m_k}{\partial t} + \nabla\cdot\left(\mathbf{U}_\mathrm{d} m_k\right) = \sum_{\alpha=1}^{N} w_\alpha g(d_\alpha)\left[\int_0^{+\infty} \beta\left(d,d_\alpha\right) d^k \,\mathrm{d}d - d_\alpha^k\right], \tag{8}$$

where the integral appearing on the right-hand side is generally solved analytically (once the functional form of β is defined).

Another underlying simplification hypothesis is that all the droplets are moving with the same velocity: $\mathbf{U}_\mathrm{d}$. This simplification is possible, for liquid-liquid dispersions, since the DSD is generally narrow enough not to have significant "size-segregation" effects. In fact, due to the close density of disperse and continuous phases and to the fact that the DSD is limited in the micrometer range, droplets of different sizes confined in a small region of the domain are characterized by velocities very close to the average droplet velocity. This simplification is not inconsistent with the use of a PBM as in different regions of the vessel, droplets might be characterized by different mean Sauter diameters, and therefore different average velocities.

2.3. Breakage kernels

Different kernels have been proposed to describe droplet breakage and one of the most popular is the CT breakage kernel (Coulaloglou and Tavlarides, 1977; Maaß and Kraume, 2012; Maaß et al., 2012):

$$g(d) = C_1\frac{\varepsilon^{1/3}}{d^{2/3}}\exp\left(-C_2\frac{\sigma}{\rho_\mathrm{c}\varepsilon^{2/3}d^{5/3}}\right), \tag{9}$$

where C_1 and C_2 are dimensionless constants (in this work $C_1 = 0.00481$ and $C_2 = 0.08$ as explained by Liao and Lucas (2009)), ε is the turbulent energy dissipation rate, ρ_c is the density of the continuous phase and σ is the interfacial tension. The kernel has been derived from the statistical turbulence theory and theoretically C_1 and C_2 are universal constants that should be valid for any fluid-fluid system. However, in its derivation some simplification hypotheses were made, impacting the accuracy of the model, and introducing some uncertainty (in turn reflected on the constants C_1 and C_2 that are no longer universal). Although clearly stated by the authors in their derivation, these simplifications are often overlooked, and it is therefore useful to list them here. It was assumed that the breakage rate depends on the turbulent energy dissipation rate only, with no other turbulence properties involved, and that the effect of viscous stresses, opposing to droplet deformation, are negligible.

In order to overcome these limitations other kernels have been proposed, such as the one adopted also in this work, namely the multifractal (MF) kernel (Baldyga and Podgórska, 1998; Podgórska, 2006b). This kernel was preferred over others since it accounts efficiently for both effects neglected by the CT kernel. As a matter of fact, the MF kernel takes into account the influence of internal intermittency on breakage and is based on the multifractal description of turbulence. Internal intermittency (i.e. large fluctuations on the turbulent dissipation rate) is responsible for scale effects and is therefore expected to play a major role in scaling up and down processes involving liquid-liquid dispersions. Last but not least, the MF kernel is consistent with the drift of the exponent on the Weber number, observed experimentally and appearing in the expression for the maximum stable droplet size.

Finally it is important to remind that the breakage mechanism considered by both the CT and MF kernel is pressure fluctuations. However, one must be aware of the possibility of simultaneous mechanisms, including droplet breakage under shear flow on the impeller blade and in the two-dimensional elongational flow field in front of the impeller blade (Kumar et al., 1998). The importance of these additional mechanisms is relevant at high values of the disperse phase volume fraction, which is not the case of this study, that considers dilute dispersions. Droplet elongation and breakup on the impeller blades is important at the very beginning of the process, when the disperse phase is introduced into the tank. This part of the process is however not modeled in this work.

In the MF kernel the fine scale structure of turbulence is taken into account. This structure is connected with vortex tube stretching, which leads to the formation of regions of space of high vorticity, surrounded by nearly irrotational fluid. Such intermittent structure of turbulence is modeled by using the multifractal turbulent theory (Frisch and Parisi, 1985; Frisch, 1995). The overall breakage rate, $g(d)$, is calculated from $g\left(d, \alpha\right)$, that in turn depends on the characteristic frequency of eddies (of scale d, equal to the droplet size) and on their activity (characterized by the singularity strength, α, also known as the scaling or multifractal exponent). Knowledge of the probability of eddy appearance, $P\left(\alpha\right)\,\mathrm{d}\alpha$, suffices for the calculation of the overall breakage rate:

$$g(d) = \int\limits_{\alpha_{\min}}^{\alpha_{\mathrm{x}}} g\left(d, \alpha\right) P\left(\alpha\right)\mathrm{d}\alpha. \tag{10}$$

The probability density, $P\left(\alpha\right)$, can be expressed for a one dimensional cut of the dissipation field (for fully developed turbulence) by the following expression (Chhabra et al., 1989; Baldyga and Podgórska, 1998):

$$P\left(\alpha\right) \approx \sqrt{\ln\left(\frac{L}{d}\right)}\left(\frac{d}{L}\right)^{1-f(\alpha)}, \tag{11}$$

where L is integral scale of turbulence and $f(\alpha)$ can be interpreted as the fractal dimension. The entire dissipation field, with energy dissipation rate over a box of size r scaling as: $\varepsilon_{\mathrm{r}} \sim \varepsilon_{\mathrm{L}}\left(r/L\right)^{\alpha-1}$, is a superposition of values between $\alpha_{\min}$ and α. The relationship between $f(\alpha)$ and α (i.e. the multifractal spectrum) can be measured and is well approximated by the following expression (Podgórska and Bałdyga, 2003):

$$f\left(\alpha\right) = a + b\alpha + c\alpha^2 + d\alpha^3 + e\alpha^4 + f\alpha^5 + g\alpha^6 + h\alpha^7 + i\alpha^8, \tag{12}$$

with $a = -3.51, b = 18.721, c = -55.918, d = 120.9, e = -162.54, f = 131.51, g = -62.572, h = 16.1, i = -1.7264$ for $\alpha \geq 0.12$. The polynomial coefficients were obtained by fitting to experimental data of Meneveau and Sreenivasan (1991).

The application of this multifractal interpretation of the fine-scale structure of turbulence results in a functional form for $g(d)$ that depends not only on the turbulence energy dissipation rate, ε, but also on the integral length-scale of turbulence L (Baldyga and Podgórska, 1998):

$$g(d) = C_{\mathrm{g}}\sqrt{\ln\left(\frac{L}{d}\right)}\frac{\varepsilon^{1/3}}{d^{2/3}}\int\limits_{\alpha_{\min}}^{\alpha_{\mathrm{x}}}\left(\frac{d}{L}\right)^{\frac{\alpha+2-3f(\alpha)}{3}} d\alpha, \tag{13}$$

where $C_{\mathrm{g}} = 0.0035$. The integral length-scale of turbulence, calculated from the following equation:

$$L = \frac{(2k/3)^{3/2}}{\varepsilon}, \tag{14}$$

allows to introduce the influence of the system scale on droplet breakage. The multifractal exponent α, which characterizes the different activity of eddies acting on droplets of diameter d, enables us to determine also the whole spectrum of stresses:

$$p\left(d, \alpha\right) \propto \rho_c \left(\varepsilon d\right)^{2/3} \left(d/L\right)^{2(\alpha-1)/3}. \tag{15}$$

The most vigorous turbulent events are labeled by α_{min} that corresponds to the most active eddies and the highest stresses; this value is known ($\alpha_{\mathrm{min}} = 0.12$) from the literature (Meneveau and Sreenivasan, 1991). The upper bound of the integral in Eq. (10) and Eq. (13), α_{x}, represents instead the weakest eddies that are still capable of breaking droplets of diameter d. This formulation of the model explains very slow breakage of small droplets resulting from decreasing α_{x} with decreasing d. The integration in Eq. (13) is performed in order to account for all possible contributions from eddies characterized by an exponent between α_{min} and α_{x}. When α_{x} approaches α_{min} then the integral in Eq. (13) approaches zero, indicating that an asymptotically stable droplet size is attained. It is important to notice that $\alpha = 1$ labels quasi-stable droplet size.

When the viscosity of the disperse phase is low, the droplet is broken if the turbulent disruptive stress due to pressure fluctuations exceeds the shape restoring stress due to the interfacial tension. In this case the weakest eddies that can disrupt the droplet are characterized by a multifractal exponent given by the following expression:

$$\alpha_x = \frac{2.5 \ln\left(\frac{L\varepsilon^{0.4}\rho_{\mathrm{c}}^{0.6}}{C_{\mathrm{x}}\sigma^{0.6}}\right)}{\ln\left(L/d\right)} - 1.5. \tag{16}$$

This equation can be applied for disperse phases with low viscosity and indeed accounts for interfacial tension effects, as the lower the interfacial tension is the smaller the stabilizing stresses are. That results in a faster breakage.

When the disperse phase viscosity is high, additional stabilizing stresses must be taken into account. Eddies are now considered vigorous enough to break the droplet if they can elongate it to such an extent that it is broken, even if it is released from the stress. The upper limit of the integral results now from the balance between pressure fluctuations, viscous stress inside the droplet and interfacial stress and, therefore, is a function of both the disperse phase viscosity, μ_{d}, and the interfacial tension, σ:

$$\alpha_x = 3\frac{\ln\left(2\left(\frac{\beta_\mu C_{\mathrm{x}}^{5/3}\mu_{\mathrm{d}}}{\rho_{\mathrm{c}}\varepsilon^{1/3}L^{1/3}d} + \sqrt{\left(\frac{\beta_\mu C_{\mathrm{x}}^{5/3}\mu_{\mathrm{d}}}{\rho_{\mathrm{c}}\varepsilon^{1/3}L^{1/3}d}\right)^2 + \frac{4C_{\mathrm{x}}^{5/3}\sigma}{\rho_{\mathrm{c}}L^{2/3}d\varepsilon^{2/3}}}\right)^{-1}\right)}{\ln\left(L/d\right)}, \qquad (17)$$

where $\beta_\mu = \frac{\ln(2)C_{\mathrm{x}}^{-5/3}}{\beta^* C_{\mathrm{p}}}$ and where $C_{\mathrm{x}} = 0.23$, $C_{\mathrm{p}} = 1.4$ and $\beta^* = 3$. This model was used to predict the droplet size evolution in stirred tanks for different liquid-liquid dispersions of low as well as high disperse phase viscosity, with or without surface active additives and with changes in the interfacial tension (Baldyga and Podgórska, 1998; Podgórska, 2005, 2006b; Bak and Podgórska, 2013; Jasińska et al., 2014).

2.4. Daughter distribution function

As it can be seen from Eq. (8) the calculation of the DSD requires knowledge of the size of the droplets that are formed during the breakage process, contained in the so-called daughter distribution function: $\beta\left(d, d'\right)$. Depending on the operating conditions, on the properties of the continuous and disperse phases and on other factors (i.e. presence of additives) different behaviors were detected, corresponding to different daughter distribution functions: Bell-shape, U-shape and M-shape. A detailed discussion on the different daughter distribution functions can be found in the work of Liao and Lucas (2009). In this work the distribution proposed by Laakkonen et al. (2006):

$$\beta\left(d, d'\right) = 180\left(\frac{d^2}{d'^3}\right)\left(\frac{d^3}{d'^3}\right)^2\left(1 - \frac{d^3}{d'^3}\right)^2, \qquad (18)$$

is employed. Equation (18) assumes that two droplets are formed in the breakage process and that symmetric breakage is the most likely event. It is useful to remind here that the daughter distribution function has a large impact on the final DSD but limited impact on the mean Sauter diameter, therefore is of secondary importance when using QMOM. Finally it is also important to remind that this choice is consistent with what proposed by Coulaloglou and Tavlarides (1977) and that when Eq. (18) is substituted into Eq. (8) an analytical solution exists for the term in between squared brackets (for $k \geq 0$):

$$\int_{0}^{+\infty} \beta\left(d, d_\alpha\right) d^k \, \mathrm{d}d - d_\alpha^k = \frac{3240 {d_\alpha}^k}{(k+9)(k+12)(k+15)} - d_\alpha^k. \tag{19}$$

Moreover, the chosen daughter distribution function results in narrow DSD and is consistent with the simplifying assumption about the uniform droplet velocity. Both breakage kernels: CT and MF, reported in Eq. (9) and Eq. (13), together with the daughter distribution function, reported in Eq. (19), were implemented with QMOM (i.e., Eq. (8)) into OpenFOAM.

3. Implementation in OpenFOAM

In this study the solver `compressibleTwoPhaseEulerFoam` of the open-source CFD code OpenFOAM-2.2.x was adopted to simulate the liquid-liquid dispersion. The solver was integrated with the PBM solved with QMOM with six moments (and therefore three nodes and three weights of quadrature). Details on the implementation of QMOM in OpenFOAM can be found in our previous work (Buffo et al., 2013a, 2014). As mentioned, in order to investigate the effect of the breakage kernel on the final predictions both the CT and MF kernels were implemented.

The Gauss-Legendre numerical integration (Golub and Welsch, 1969) method was adopted to calculate the integral appearing in the MF kernel reported in Eq. (13). Due to the integrand's complexity, adequate Gauss-Legendre nodes should be selected in order to have an acceptable trade-off between computational time and accuracy. In this work five Gauss-Legendre nodes were employed.

The governing equations were solved by the PIMPLE (merged PISO-SIMPLE) algorithm implemented in OpenFOAM. As well known, it is efficient for simulating transient incompressible or compressible flows with large time-steps. The main difference between the PIMPLE algorithm, when compared with the SIMPLE and PISO algorithm is that it allows under-relaxation during each time step, improving numerical robustness, and allowing the use of large Courant numbers (and therefore large time steps which is suitable for this work). More details about the PIMPLE algorithm can be found in Passalacqua and Fox (2011).

CFD and PBM can be linked together by using different strategies, depending on the phase coupling. In some multi-phase systems, characterized by tight phase-coupling CFD and PBM need to be updated at each time step, following this procedure (mainly adopted in all our previous works):

1. First the equation for the volume fraction of the disperse phase is solved together with the turbulence model equations.
2. Abscissas and weights of quadrature are calculated from the initial values of the six moments of the DSD; subsequently the right-hand side of Eq. (8) is also calculated and the equation for the moment of order k can now be solved.
3. From the updated values of the moments of the DSD the mean Sauter diameter is calculated, allowing for the evaluation of the interfacial force and the subsequent solution of the momentum balance and Poisson pressure equations.
4. The iterative procedure is repeated from point 1.

However, being the disperse phase quite dilute, the system is characterized by a weak coupling between CFD and PBM. This can be easily quantified by computing a characteristic mixing time, as for example the ratio between the turbulent kinetic energy and the turbulent dissipation rate in the vessel, and a characteristic breakage time, as the inverse of the breakage kernel (Marchisio et al., 2006). By using proper characteristic values for the variables involved the mixing time-scale is evaluated to be smaller than 0.1-0.01 s, whereas the breakage time time-scale larger than 1-10 s, confirming that for these specific test cases mixing is faster than breakage. These time-scale can also be used to define the following strategy to operate the "weak coupling" between TFM and PBM.

At first only the governing equations of the TFM were solved, to obtain the steady-state flow field information (with a fixed mean Sauter diameter chosen a-priori). Then the TFM governing equations are disabled, the flow and turbulent fields "frozen" and the PBM is solved for a number of time steps. Every fixed number of time steps the flow field is updated, based on the new mean Sauter diameter value, but once a pseudo-steady-state for the flow field is reached, the TFM equations are frozen again. Based on the time-scale analysis it was decided that for every second of actual simulated time with the PBM, only 0.1 seconds of PBM with TFM were also simulated. This optimal is valid for the geometries and operating conditions investigated in this work; however, different systems might have different optimal solution strategies.

4. Test cases and numerical details

In order to investigate the capability of the CT and MF kernels to simulate droplet breakage the three different stirred tanks described in Table 1 and Fig. 1 were simulated, under the operating conditions and with the continuous and disperse phases reported in Table 2.

	H	T	D	W
T1	0.300	0.242	0.075	0.0242
T2	0.175	0.151	0.047	0.0151
T3	0.150	0.150	0.075	0.0150

Table 1: Geometry characteristics of the three stirred tanks investigated in this work. H is height of tank (m), T is the diameter of the tank (m), D is the diameter of the impeller (m), W is the width of the baffles (m).

	Geometry	μ_c	μ_d	ρ_c	ρ_d	σ	ϕ_d	N
Case 1	T1	1.00	0.72	998	1022	0.0250	0.0020	300
Case 2	T2	1.00	0.72	998	1022	0.0250	0.0020	392
Case 3	T3	0.89	10.00	997	946	0.0458	0.0038	240
Case 4	T3	0.89	10.00	997	946	0.0458	0.0038	350
Case 5	T3	0.89	100.0	997	985	0.0464	0.0038	300
Case 6	T3	0.89	100.0	997	985	0.0464	0.0038	350
Case 7	T3	0.89	500.0	997	973	0.0505	0.0038	300
Case 8	T3	0.89	500.0	997	973	0.0505	0.0038	350

Table 2: Fluid properties and operating conditions investigated in this work: μ_c is the viscosity of the continuity phase (mPas), μ_d is the viscosity of the dispersed phase (mPas), ρ_c is the density of continuity phase (kg m^{-3}), ρ_d is the density of dispersed phase (kg m^{-3}), σ is the surface tension between the two phases (Nm), ϕ_d is the global disperse phase volume fraction (-) and N is the impeller rotational speed (rpm).

In total eight cases were investigated in this work. Case 1 is exactly the geometrical scale up of the Case 2, the scaling factor calculated from the

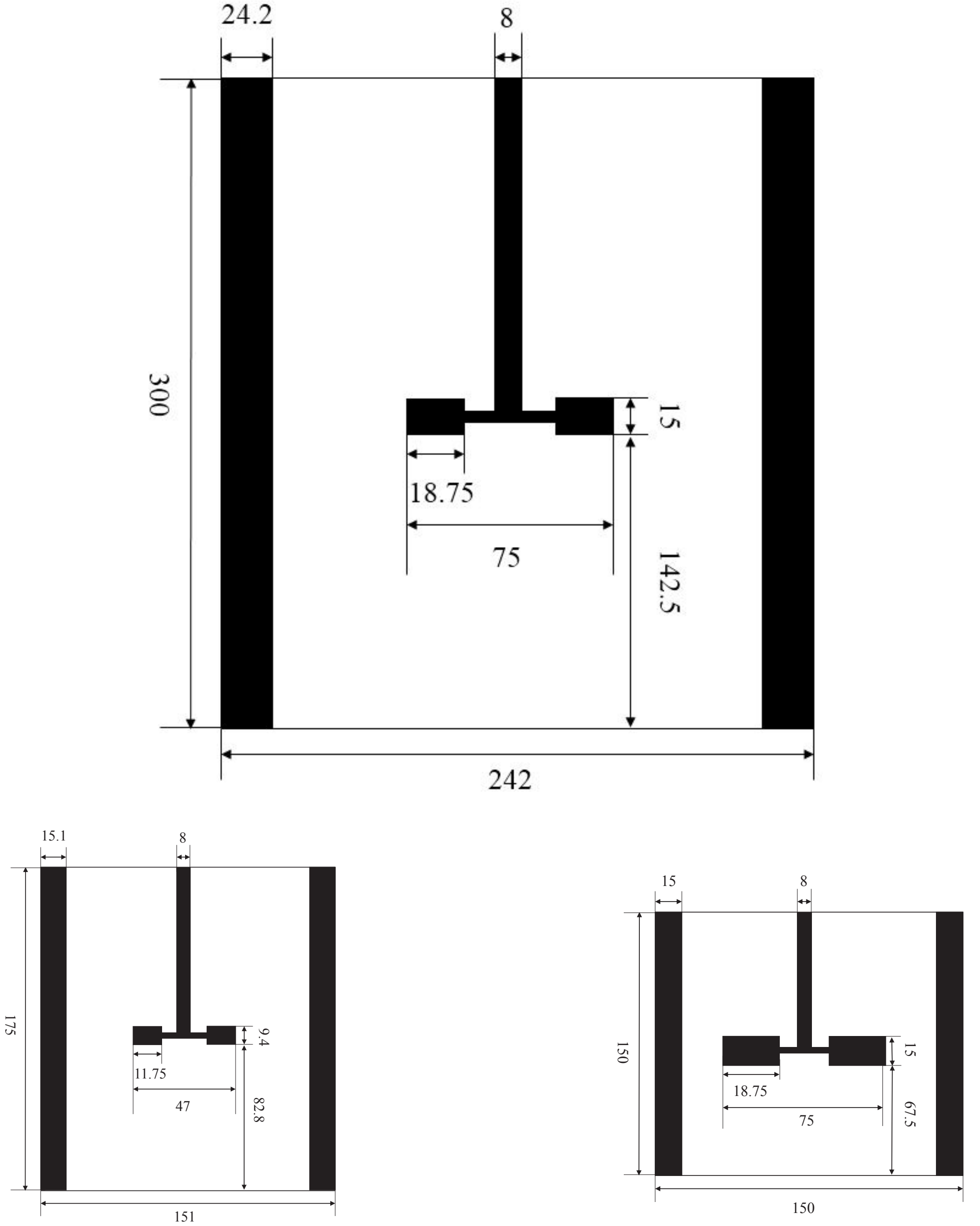

Figure 1: Geometry of the stirred tanks investigated in this work: T1 (top), T2 (bottom left) and T3 (bottom right). The unit is mm.

length of the tank is 1.71. The stirring speed was adjusted so that the power input per unit mass was exactly the same, resulting in the same (for Cases 1 and 2) experimentally measured Power number. Cases 3 to 8 were carried out in a different geometry (T3) characterized by a larger impeller diameter to tank diameter ratio and under different stirring rates and viscosities of the disperse phase. In particular, in Cases 3 and 4, 5 and 6, 7 and 8, three silicone oils differing in viscosity were considered. They, however, differ slightly in interfacial tension (see Table. 2). Measured interfacial tension values for silicone oils of viscosity 10 mPas and 100 mPas are very similar (the difference is only 1.3%) and the difference between the smallest and largest σ for silicone oils is also not very large.

Experiments were performed in completely filled tanks enclosed by stainless steel cover. In Cases 1 and 2 dispersion samples were withdrawn from the tank, placed on microscope slide and stabilized with sodium dodecyl sulfate (SDS). A high resolution digital camera was used to capture droplet images from a microscope. Very good quality of obtained images allowed automatic droplet size analysis using Visilog software. In Cases from 3 to 8 the dispersion was monitored on-line. The stirred tank was placed in a square jacked to avoid optical distortion. High resolution digital camera RETIGA EX mounted on a stereo microscope objective was used in experiments. Exposure time was set to 15 μm, StreamPix 2.1.1 was applied to capture droplet images and Image Pro Plus 4.5 was used to determine the DSD. Measurements were performed by placing three points on the droplet perimeter. The number of drops used per each droplet size distribution was about 800-1000. The original experimental data for the first two cases can be found in the work of Podgórska (2006a), corresponding to an experimentally measured Power number of 6.0, whereas the last six cases can be found in the work of Podgórska (2006b), corresponding to an experimentally measured Power number of 5.5.

The different computational meshes, discretizing only half of the geometry by means of periodic boundary conditions, were generated with Ansys ICEM and then exported into the OpenFOAM environment. The motion of the stirrer was modelled by using the Multiple Reference Frame (MRF) approach (Luo et al., 1994).

The final number of cells for the computational grids of T1 and T2 was exactly the same, corresponding to 170,413 hexahedral cells. The final number of cells for the computational grid of T3 was 168,910 again with hexahedral cells. All the impellers and baffles in each computational grid were repre-

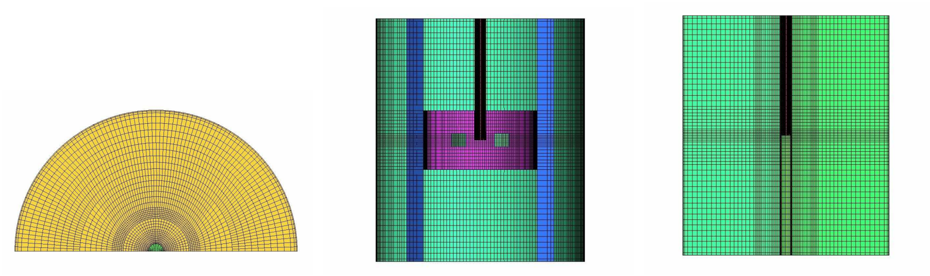

Figure 2: Final computational mesh used for T1.

sented as zero-thickness objects; this simplification was considered acceptable as rendering the thickness of these objects increased significantly the computational costs but did not affect appreciably the final predictions. Sketch of the final mesh for T1 are reported in Fig. 2. For all these test cases the final meshes were found to be sufficiently fine to characterize the flow and turbulent fields, as resulted from the grid independence analysis conduced in this work and reported in Table 3. The table reports, only for Case 2, the comparison between the experimentally measured Power number and the Power number predicted by the CFD code, calculated from the torque:

$$\text{Po} = \frac{2\pi(N/60)T_q}{\rho_c(N/60)^3 D^5}, \tag{20}$$

and from the volume-average turbulent dissipation rate:

$$\text{Po} = \frac{\bar{\varepsilon}V}{(N/60)^3 D^5}. \tag{21}$$

In the above equations T_q is the torque applied to the stirrer and $\bar{\varepsilon}$ is the volume-average dissipation rate in the tank. The corresponding numbers for the other test cases are omitted as they are very similar. Closer observation of Table 3 reveals that by increasing the number of cells in the mesh, the Power number calculated from the torque becomes closer and closer to the experimental value, and that a number of cells equal to 170k results in reasonable agreement. It is also worth mentioning that the mismatch between the Power number calculated from the torque applied to the stirrer and from the torque applied to the walls of the vessel becomes negligible only at this level of grid refinement.

N. of cells	Po (torque)	Po ($\bar{\varepsilon}$)	Po (experimental)
25k	2.65	1.7	6
110k	4.82	3.0	
170k	4.84	3.1	
390k	4.90	3.2	

Table 3: Grid independence investigation for Case 2. For all the different cell numbers Po (torque) is calculated from Eq. (20), Po(ε) is calculated from Eq. (21) whereas Po (experimental) is the corresponding experimental measurement.

It is also worth pointing out that the Po calculated from Eq. (21) is always underestimated and grid refinements seem not to help much. As well known this problem comes from the shortcomings of the turbulence model adopted in this work, which underpredicts the turbulence dissipation rate in the discharge region of disk turbine impeller. Similar underestimations when using the RANS approach can be found in the literature (Montante et al., 2001; Paul et al., 2004), whereas only when using large eddy simulation (LES) predictions seem in accordance with experimental data (Aubin et al., 2004). This underestimation poses a serious problem to our simulations, as the breakage kernel depends also on the turbulent dissipation rate. Underestimating the turbulence dissipation rate means underestimating the breakage rate, hindering the capability of the approach to simulate the evolution of the DSD. In order to overcome this problem, and because the underestimation of the turbulent dissipation rate is a well known problem, a correction for the turbulent dissipation rate, $\varepsilon_{\text{corr}}$, consistently applied to all the investigated kernels, is introduced in this work. $\varepsilon_{\text{corr}}$ is calculated from Eq. (22):

$$\varepsilon_{\text{corr}} = \frac{\text{Po}_{\text{exp}}}{\text{Po}_{\text{CFD}}}, \tag{22}$$

where Po_{exp} is experimentally measured Power number, Po_{CFD} is Power number calculated from CFD. The correction scales the turbulent dissipation rate field of a factor, in order to match the experimentally measured Power number. The specific $\varepsilon_{\text{corr}}$ values used in this study are reported in Tab. 4 and range between 1.4 and 1.9. Although this empirical and simple approach seems to affect the predictive power of the adopted methodology, it is a necessary measure until more sophisticated turbulence models are developed. In addition this correction is applied only when the turbulence dissipation rate is employed inside the PBM, namely in the CT kernel of Eq. (9) and in the MF kernel of Eq. (13).

	$\mathrm{Po}_{\mathrm{exp}}$	$\mathrm{Po}_{\mathrm{CFD}}$	$\varepsilon_{\mathrm{corr}}$
Case 1	6.0	4.2	1.43
Case 2	6.0	3.1	1.94
Case 3	5.5	3.9	1.41
Case 4	5.5	3.8	1.45
Case 5	5.5	3.8	1.45
Case 6	5.5	3.8	1.45
Case 7	5.5	3.8	1.45
Case 8	5.5	3.8	1.45

Table 4: Correction for the turbulent dissipation rate ($\varepsilon_{\mathrm{corr}}$, -) used in Cases 1 to 8.

An overview of the numerical schemes and of boundary conditions used in this work can be found in Table 5.

Variable	Scheme	Boundary conditions at walls
Droplet vol. frac.	Second-order TVD scheme with vanLeer flux limiter	Zero grad.
Droplet velocity	Second-order TVD scheme with vanLeer flux limiter	No-slip
Cont. liquid velocity	Limited second-order central scheme	No-slip
Pressure	Limited second-order central scheme	Zero grad.
k	Limited second-order central scheme	Std. wall func.
ε	Limited second-order central scheme	Std. wall func.
Moments	First-order upwind	Zero grad.

Table 5: Numerical schemes used in the test cases.

5. Results and discussion

Let us start by analyzing the comparison between the frequency of breakup predicted by the CT kernel and the MF kernel, plotted in Fig. 3 as a function of droplet size, for different values of the turbulent dissipation rate, ε, turbulent kinetic energy, k and viscosity of the disperse phase, μ_{d}. The other fluid properties are taken from Table 2 and correspond to Case 4. It is worth pointing out that the predictions for the CT kernel are identical for different values of the viscosity of the disperse phase, since there is no explicit dependency in the kernel formulation. For this reason the predictions for $\mu_{\mathrm{d}} = 10$ mPas and for $\mu_{\mathrm{d}} = 500$ mPas result in one single line (dashed blue line). On the contrary for the MF kernel, the two viscosity values result in very different trends for the breakage frequency, as depicted by the continuous and dashed red lines in Fig. 3. In fact, MF kernel contains the dependency on the viscosity of the dispersed phase as shown in Eq. (17).

It should be remarked, moreover, that the CT kernel depends only on the turbulent dissipation rate and not on other turbulent quantities. This means that if the PBM is solved via a lumped zero-dimensional model for different systems, characterized by the same ε but for example by different k, the results in terms of breakage rate predictions will be exactly the same. Again only using the MF kernel other turbulence effects such as intermittency that affects the breakage rate will be taken into account even in lumped zero-dimensional models.

The experiments of liquid-liquid systems in stirred tanks are usually carried out by starting with the disperse phases not fully dispersed yet. The detailed methods about how the disperse phase is introduced into the continuous phase can be found in the work of Podgórska (2006a,b). The spirit of the methodology adopted in the experiments is that the disperse phase is introduced by using a long needle just above the impeller. In such a way the freshly added disperse phase is prevented from sticking to the upper tank plate. The disperse phase is then fed until the desired global disperse phase volume fraction is reached, but no information regarding the initial DSD is available from the experiments. Therefore, simulations with different initial DSDs were performed, in order to estimate the effect of this input parameter on the final time evolution of the mean Sauter diameter. Results, corresponding to Cases 1 and 2, are reported in Fig. 4 for initial mean Sauter diameters of 520 μm and 110 μm and for the CT kernel. As it is seen both simulations converge, after 2000 seconds, to the same mean Sauter diameter, showing

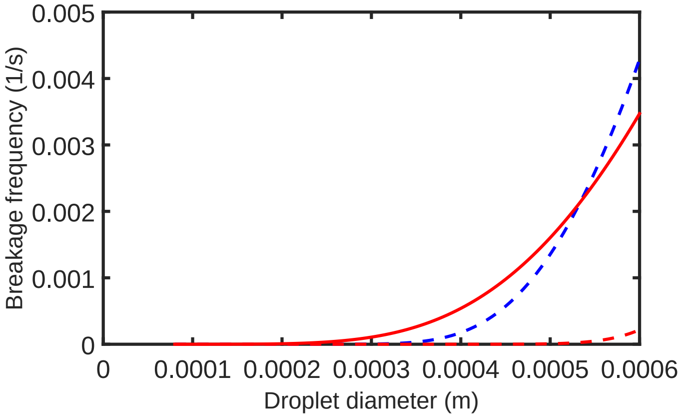

Figure 3: Breakage frequency/kernel versus droplet diameter for CT kernel with $\mu_{\mathrm{d}} = 10$ mPas and 500 mPas and $\varepsilon = 0.1\ \mathrm{m^2s^{-3}}$ (dashed blue line), for MF kernel with $\mu_{\mathrm{d}} = 10$ mPas, $\varepsilon = 0.1\ \mathrm{m^2s^{-3}}$ and $k = 0.1\ \mathrm{m^2s^{-2}}$ (solid red line) and for MF kernel with $\mu_{\mathrm{d}} = 500$ mPas, $\varepsilon = 0.1\ \mathrm{m^2s^{-3}}$ and $k = 0.1\ \mathrm{m^2s^{-2}}$ (dashed red line).

therefore that the effect of the initial mean Sauter diameter is marginal, if a sufficiently long time interval is simulated.

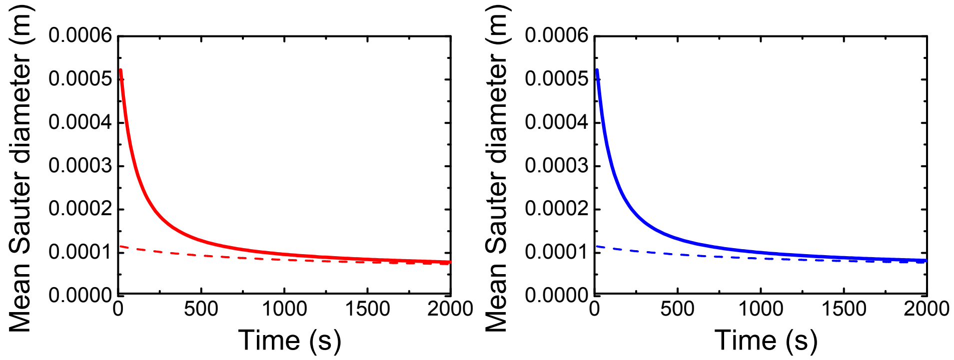

Figure 4: Time evolution of the mean Sauter diameter predicted with the CT kernel for Case 1 (left) and Case 2 (right) starting from an initial mean Sauter diameter of 110 μm (dashed line) and 520 μm (solid line).

Next, the time evolutions for the mean Sauter diameter predicted with the CT and MF kernels for Cases 1 and 2 are compared with experimental data in Fig. 5. In the experiment the agitation lasted for 5 hours, but the

Sauter Mean diameter tended to converge after 1 hour. Hence, simulations are reported in the figure only for 2000 seconds, although in some case longer times were also simulated (i.e. 7200 seconds). The initial diameter was 520 μm for both cases and both kernels result in acceptable agreement with experiments. As it can be seen, the predictions of the final mean Sauter diameter with the CT and MF kernels are very similar for the large tank and small tank, whereas a slightly larger difference is detected for the MF kernel. This is because in the MF kernel the effect of local intermittency is considerd. It is also seen that droplet sizes predicted by MF model are still decreasing very slowly because very rare but very strong stresses are capable to break small droplets.

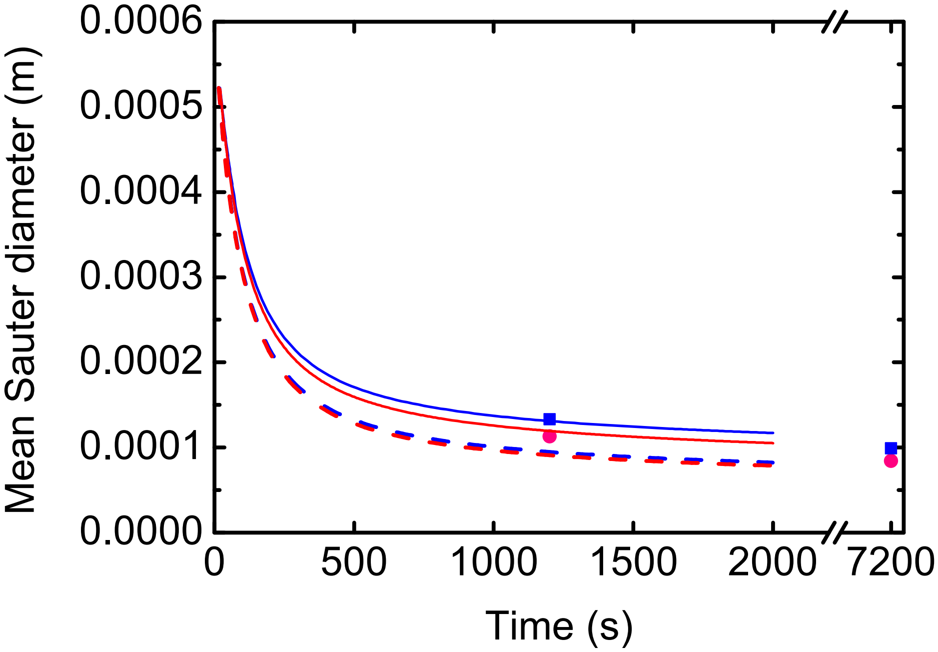

Figure 5: Comparison of the time evolution of the mean Sauter diameter predicted by the CT kernel (dashed line) and the MF kernel (continuous line) for Case 1 (red line) and Case 2 (blue line) with experimental values for Case 1 (red circle) and Case 2 (blue square). The simulation's plot is cut after 2000 seconds

It is important to stress here that Cases 1 and 2 correspond to two geometrically similar tanks, operating at different stirring rates, so that the global power input per unit mass is exactly the same. This is confirmed by our simulations, that show for the two cases the very same volume-averaged turbulent dissipation rate, $\bar{\varepsilon}$. If this value was used in two lumped zero-dimensional simulations for Cases 1 and 2 the very same results would have been obtained with the CT kernel, whereas only using the MF kernel different results would have been obtained. The fact that the CFD-PBM predictions are different for Cases 1 and 2 also with the CT kernel is due to the fact that the two tanks are characterized by the same volume-averaged turbulent dissipation rate, $\bar{\varepsilon}$, but by different turbulent dissipation rate distributions in the T1 and T2 geometries. This is evidenced in Fig. 6, where among other variables, contour plots of the turbulent dissipation rate are reported. As it is seen, although Cases 1 and 2 correspond to the same $\bar{\varepsilon}$, locally some differences in ε are observed, resulting in different predictions for the mean Sauter diameter. These differences in the local ε values, come with different predictions also for the turbulent kinetic energy, k, and for the velocity magnitude, $\mathbf{U}_\mathrm{d}$ and $\mathbf{U}_\mathrm{c}$, resulting therefore in even larger differences when the MF kernel is used.

It is now interesting to consider the contour plots for the disperse phase volume fraction, α_d, and the mean Sauter diameter, d_{32}, reported in Fig. 7. As it is seen for both CT and MF kernels the contour plots shape are quite similar. Besides this, for both Cases 1 and 2 the disperse phase is quite homogeneously distributed and the mean Sauter diameter is also quite uniform in the vessels. This is an interesting result that shows that under these operating conditions mixing in the vessel is quite fast and capable of distributing the droplets around. This implies that, under these operating conditions, mixing is capable of quickly homogenizing the gradients created by the breakup process. In other words breakup is still very strong around the impeller and almost null far away from it, but mixing is making the dispersion homogeneous. This however does not mean that these two cases could be well simulated by a zero-dimensional model, that considers only one value of the turbulent dissipation rate (e.g. $\bar{\varepsilon}$), as the interplay between mixing and breakup would be totally neglected, and more importantly the fact that different regions of the vessels operate under different breakup rates would be completely overlooked.

Let us now consider Cases 3 to 8, where different viscosities of the disperse phase are considered at different stirring rates. For these simulations the initial mean Sauter diameters were equal to the experimental data after five minutes of stirring. The initial mean Sauter diameters of these cases are respectively: 0.232, 0.122, 0.243, 0.204, 0.557 and 0.404 mm. First we

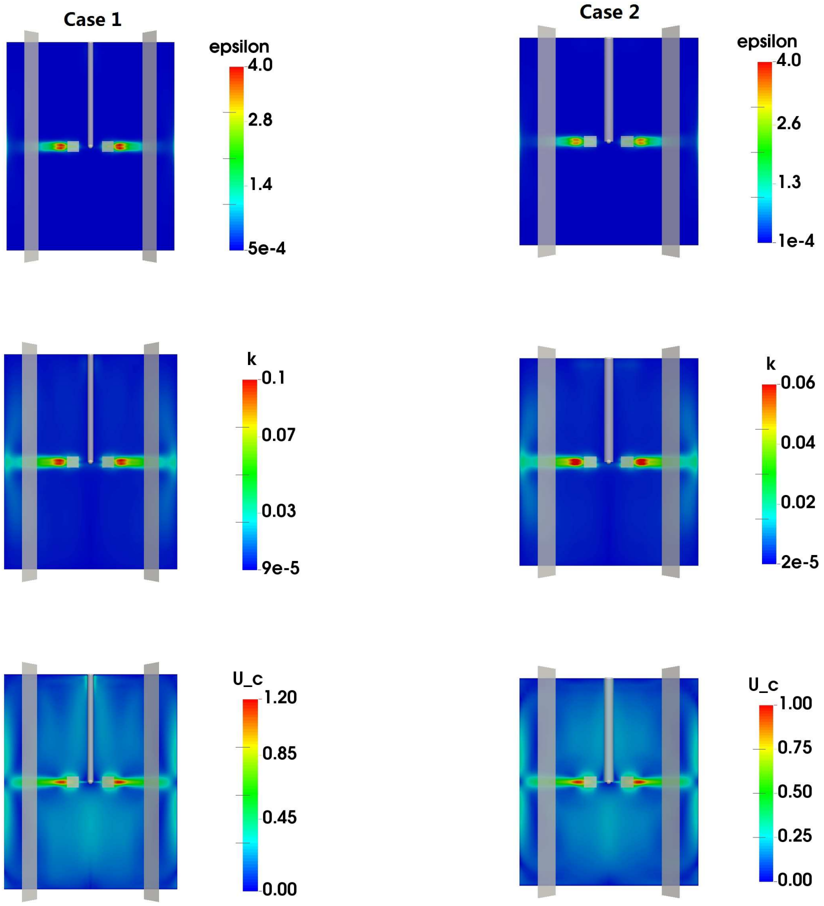

Figure 6: Contour plots from top to bottom of turbulent energy dissipation rate (ε, m^2 s^{-3}), turbulent kinetic energy (k, m^2 s^{-2}) and continuous phase velocity magnitude ($\mathbf{U}_\mathrm{c}$, m s^{-1}) for Case 1 (left) and Case 2 (right) at 2000 seconds.

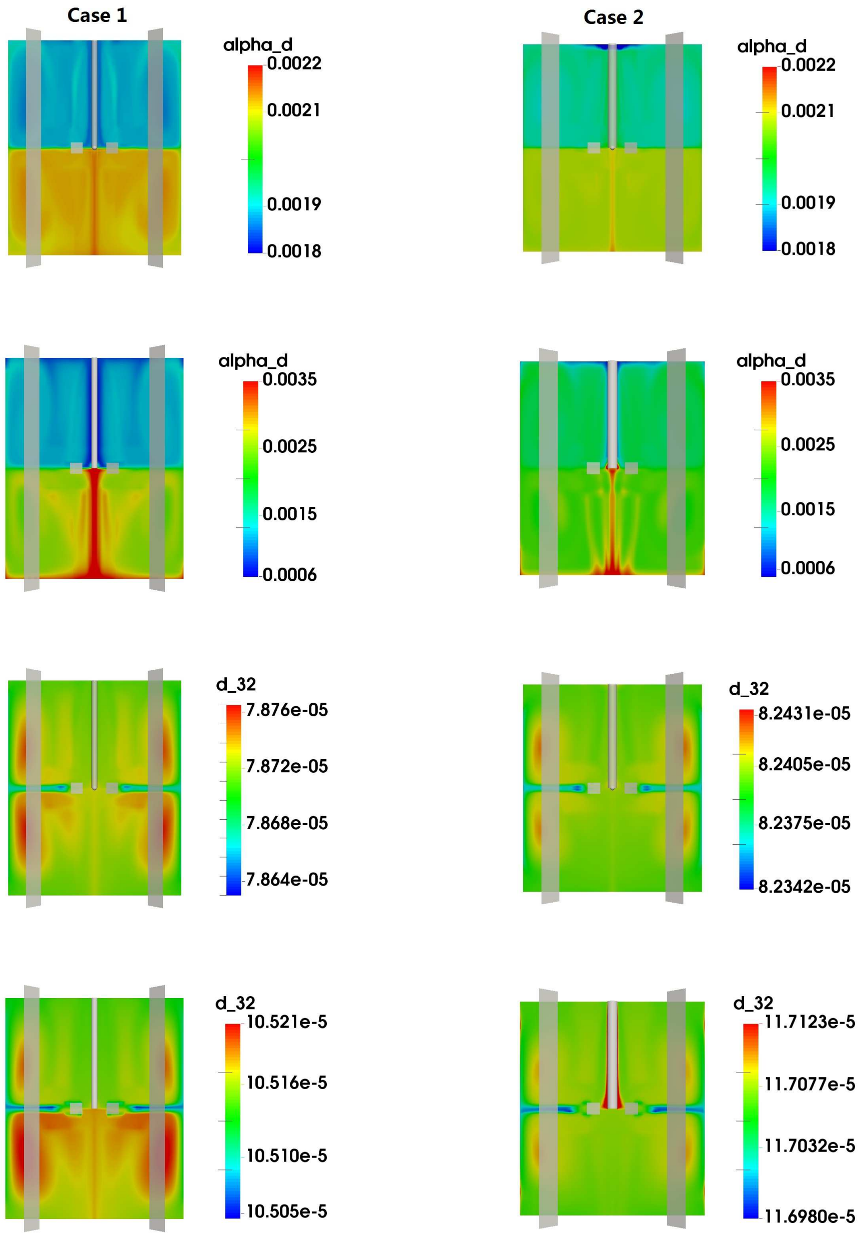

Figure 7: Contour plots from top to bottom of the disperse phase volume fraction (α_{d}, -) by CT kernel (first row) and MF kernel (second row), and mean Sauter diameter (d_{32}, m) by CT kernel (third row) and MF kernel (fourth row) for Case 1 (left) and Case 2 (right) at 2000 seconds.

consider Cases 3 and 4 where another value for the viscosity ($\mu_{\mathrm{d}} = 10$ mPas) of disperse phase is investigated at two stirring rates. The comparison with experiments of the predictions of the CT and MF kernels is reported in Fig. 8. As expected, for the higher stirring rate the predicted (experimentally measured and simulated) mean Sauter diameters are smaller. Both kernels can predict good agreement with experiments, with the predictions obtained with the CT kernel reaching slightly smaller values.

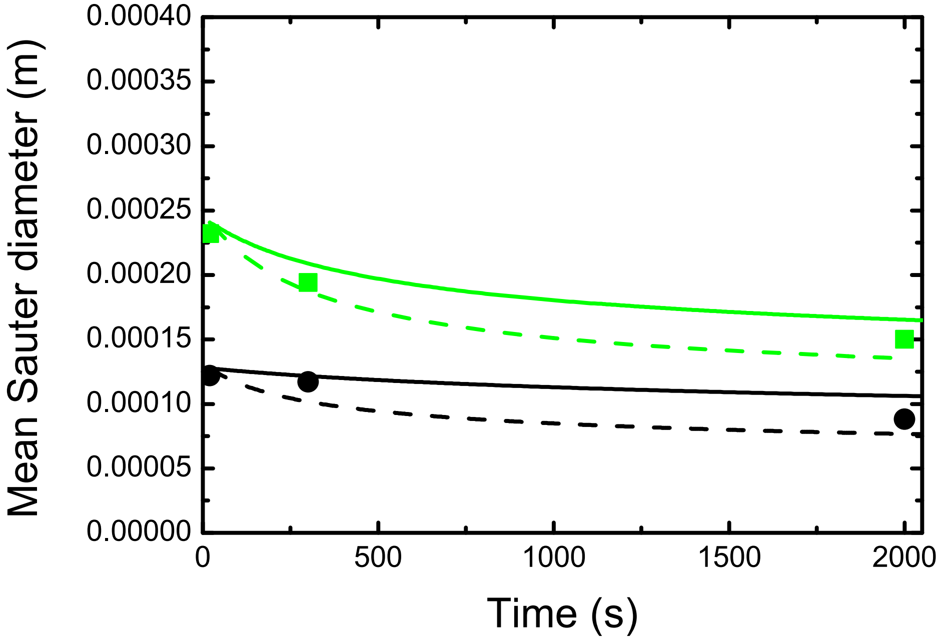

Figure 8: Comparison of the time evolution of the mean Sauter diameter predicted by the CT kernel (dashed line) and the MF kernel (continuous line) for Case 3 (green line) and Case 4 (black line) with experimental values for Case 3 (green square) and Case 4 (black circle).

In Cases 5 and 6 a higher viscosity for the disperse phase ($\mu_{\mathrm{d}} = 100$ mPas) is investigated, whereas in Cases 7 and 8 an even higher value ($\mu_{\mathrm{d}} = 500$ mPas) is considered. The predictions of the CT and MF kernels of Cases 5 and 6, 7 and 8 at different stirring rates are compared in Fig. 9 and Fig. 10 with experimental data. As it can be seen for these four cases only the MF kernel results in decent agreement with experiments, whereas predictions obtained with the CT kernel severely underestimate the mean Sauter diameter.

As mentioned this is due to the fact that the CT kernel does not account for the viscosity effects of the disperse phase. As a matter of fact, the final mean Sauter diameter value predicted by CT kernel for Case 8 tends to be the same of those predicted in Cases 4 and 6, since Cases 4, 6 and 8 are operated under the same stirring rate, which results in similar turbulent dissipation rate values, $\bar{\varepsilon}$. Additional contour plots for Cases 7 and 8 are reported in Fig. 11. As it is seen for both Cases 7 and 8 the disperse phase is not quite homogeneous (compared to Cases 3 and 4) as it accumulates at the top of the tank surrounding the impeller shaft. This implies that for a high viscosity of the disperse phase, droplets are not easy to break; these large droplets tend to accumulate at the top as a consequence of the buoyancy force and as confirmed by visual observation conducted during experiments.

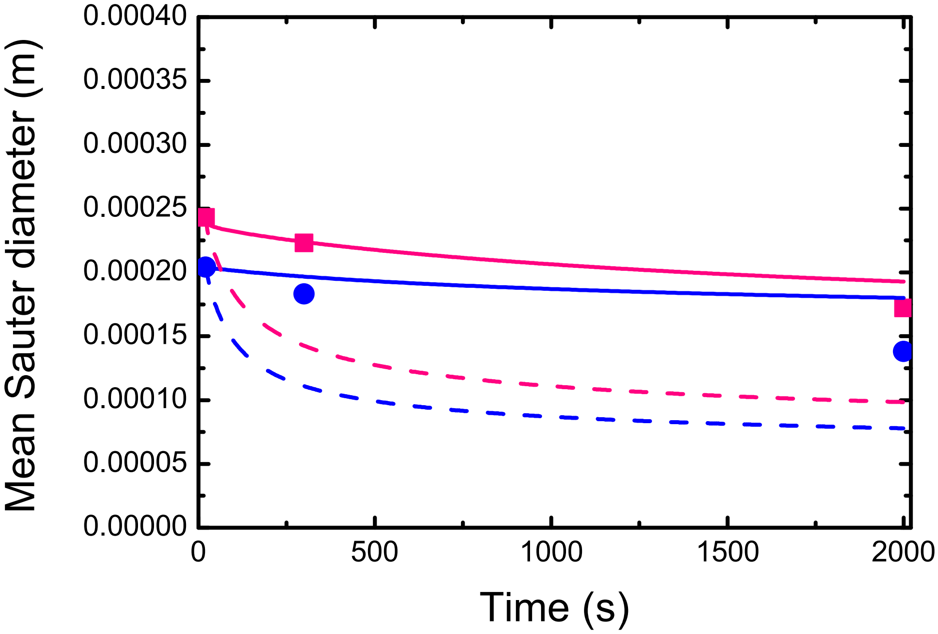

Figure 9: Comparison of the time evolution of the mean Sauter diameter predicted by the CT kernel (dashed line) and the MF kernel (continuous line) for Case 5 (red line) and Case 6 (blue line) with experimental values for Case 5 (red square) and Case 6 (blue circle).

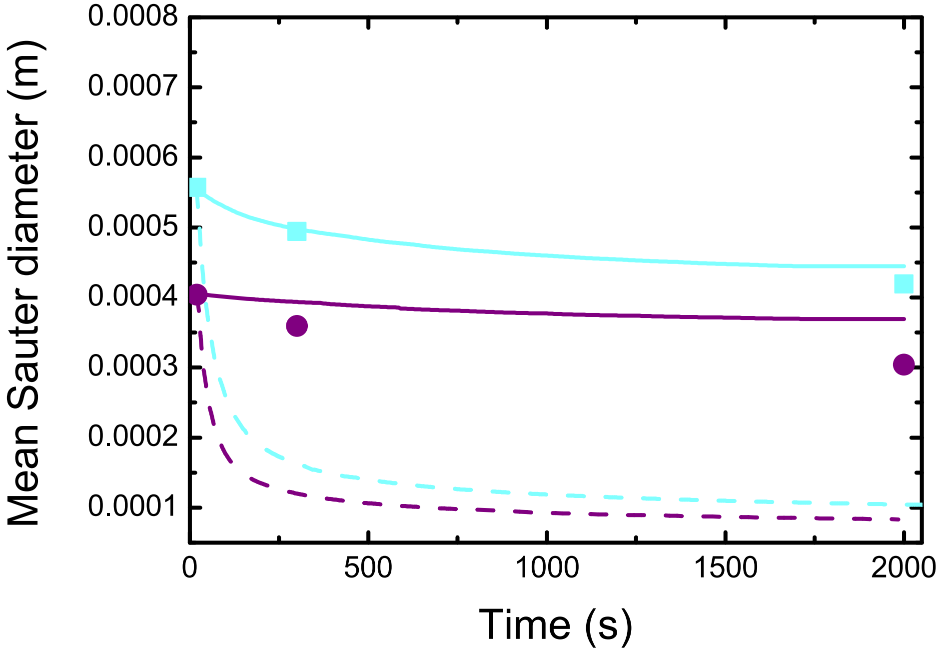

Figure 10: Comparison of the time evolution of the mean Sauter diameter predicted by the CT kernel (dashed line) and the MF kernel (continuous line) for Case 7 (light blue line) and Case 8 (purple line) with experimental values for Case 7 (light blue square) and Case 8 (purple circle).

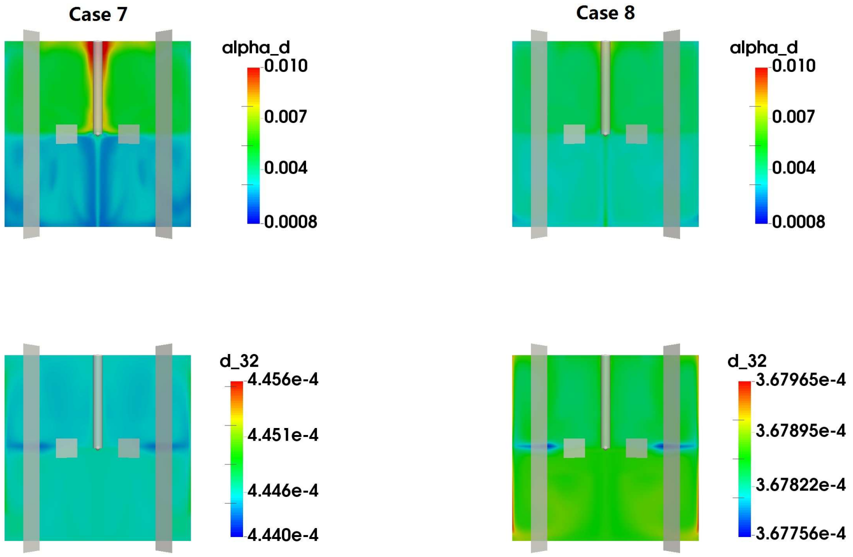

Figure 11: Contour plots from top to bottom of the disperse phase volume fraction (α_{d}, -) and mean Sauter diameter (d_{32}, m) with MF kernel for Case 7 (left) and Case 8 (right) at 2000 seconds.

6. Conclusions

In this work, the TFM is coupled with the PBM, solved with QMOM, to simulate turbulent liquid-liquid dispersion undergoing breakage. Two different breakage kernels (the CT and the MF kernels) were adopted in our simulations, performed with the open-source CFD code OpenFOAM. Eight different test cases were simulated in three geometrically different tanks working under different operating conditions and with different continuous and disperse phases, in order to investigate scale-up and disperse phase viscosity effects. Eventually the mean Sauter diameters calculated from the CT kernel and MF kernel were compared with experimental data, providing our simulations with the necessary validation.

Our CFD results show that, for dilute systems, the disperse phase is distributed rather homogeneously and that the mean Sauter diameter is uniform in the vessel. As the turbulent intermittency phenomenon is considered in the MF kernel, it can predict larger mean Sauter diameter differences, compared with the CT kernel, when dealing with scale-up operations. Both the CT and MF kernels are capable of adequately describing the mean Sauter diameter predictions for operations with low viscosity disperse phase, however the CT kernel underpredicts the mean Sauter diameter when dealing with high viscosity disperse phases, whereas the MF kernels results in satisfactory predictions. Last but not least, the MF kernel contains universal constants that were derived from theory and need not to be changed when simulating other systems.

In our future work we will consider test cases characterized by higher volume fractions, where the effect of coalescence is no more negligible. Moreover the problem of adequately describing, with lumped zero-dimensional models, droplet breakage in large stirred tanks will also be investigated.

Acknowledgments

The research stay at Politecnico di Torino of Dongyue Li was supported by the Chinese Scholarship Council (CSC, No. 201406880003) and of Wioletta Podgórska by the European Union in the framework of the European Social Fund through the Warsaw University of Technology Development Program. All the authors thank Jeremias De Bona for fruitful discussions.

References

V. Alopaeus, J. Koskinen, K.I. Keskinen, and J. Majander. Simulation of the population balances for liquid–liquid systems in a nonideal stirred tank. Part 2–Parameter fitting and the use of the multiblock model for dense dispersions. *Chemical Engineering Science*, 57:1815–1825, 2002.

M.M. Attarakih, C. Drumm, and H. Bart. Solution of the population balance equation using the sectional quadrature method of moments (SQMOM). *Chemical Engineering Science*, 64:742–752, 2009.

M.M. Attarakih, M. Hlawitschka, M. Abu-Khader, S. Al-Zyod, and H. Bart. CFD-population balance modelling and simulation of coupled hydrodynamics and mass transfer in liquid extraction columns. *Applied Mathematical Modelling*, 39:5105–5120, 2015.

J. Aubin, D.F. Fletcher, and C. Xuereb. Modeling turbulent flow in stirred tanks with CFD: the influence of the modeling approach, turbulence model and numerical scheme. *Experimental thermal and fluid science*, 28:431–445, 2004.

A. Bak and W. Podgórska. Drop breakage and coalescence in the toluene/water dispersions with dissolved surface active polymers PVA 88% and 98%. *Chemical Engineering Research and Design*, 91:2142–2155, 2013.

J. Baldyga and W. Podgórska. Drop break–up in intermittent turbulence: Maximum stable and transient sizes of drops. *The Canadian Journal of Chemical Engineering*, 76:456–470, 1998.

P.J. Becker, F. Puel, H.A. Jakobsen, and N. Sheibat-Othman. Development of an improved breakage kernel for high dispersed viscosity phase emulsification. *Chemical Engineering Science*, 109:326–338, 2014.

A. Behzadi, R.I. Issa, and H. Rusche. Modelling of dispersed bubble and droplet flow at high phase fractions. *Chemical Engineering Science*, 59: 759–770, 2004.

A. Buffo and D.L. Marchisio. Modeling and simulation of turbulent polydisperse gas-liquid systems via the generalized population balance equation. *Reviews in Chemical Engineering*, 30:73–126, 2014.

A. Buffo, D.L. Marchisio, M. Vanni, and P. Renze. Simulation of polydisperse multiphase systems using population balances and example application to bubbly flows. *Chemical Engineering Research and Design*, 91:1859–1875, 2013a.

A. Buffo, M. Vanni, D.L. Marchisio, and R.O. Fox. Multivariate quadrature-based moments methods for turbulent polydisperse gas–liquid systems. *International Journal of Multiphase Flow*, 50:41–57, 2013b.

A. Buffo, D.L. Marchisio, and M. Vanni. On the implementation of moment transport equations in openfoam to preserve conservation, boundedeness and realizability. In *International Conference on Multiphase Flows in Industrial Plants, Sestri Levante, September 16-19*, 2014.

J.C. Cheng, R.D. Vigil, and R.O. Fox. A competitive aggregation model for Flash NanoPrecipitation. *Journal of colloid and interface science*, 351: 330–342, 2010.

A.B. Chhabra, C. Meneveau, R.V. Jensen, and K.R. Sreenivasan. Direct determination of the $f(\alpha)$ singularity spectrum and its application to fully developed turbulence. *Physical Review A*, 40:5284–5294, 1989.

Y.G. Cho and M.R. Kamal. Effect of the dispersed phase fraction on particle size in blends with high viscosity ratio. *Polymer Engineering & Science*, 42:2005–2015, 2002.

C.A. Coulaloglou and L.L. Tavlarides. Description of interaction processes in agitated liquid–liquid dispersions. *Chemical Engineering Science*, 32: 1289–1297, 1977.

D.A. Drew. Mathematical modeling of two–phase flow. Technical report, DTIC Document, 1982.

D.A. Drew and S.L. Passman. *Theory of multicomponent fluids*, volume 135. Springer, 2006.

C. Drumm, M.M. Attarakih, and H. Bart. Coupling of CFD with DPBM for an RDC extractor. *Chemical Engineering Science*, 64:721–732, 2009.

J.L. Favero, L.F.L.R. Silva, and P.L.C. Lage. Modeling and simulation of mixing in water-in-oil emulsion flow through a valve-like element using a population balance model. *Computers & Chemical Engineering*, 75:155–170, 2015.

U. Frisch. *Turbulence: the legacy of AN Kolmogorov*. Cambridge University Press, 1995.

U. Frisch and G. Parisi. On the singularity structure of fully developed turbulence. In *Proceedings of The International School of Physics "Enrico Fermi", Amsterdam*, 1985.

A. Gäbler, M. Wegener, A.R. Paschedag, and M. Kraume. The effect of pH on experimental and simulation results of transient drop size distributions in stirred liquid–liquid dispersions. *Chemical Engineering Science*, 61:3018–3024, 2006.

G.H. Golub and J.H. Welsch. Calculation of gauss quadrature rules. *Mathematics of Computation*, 23:221–230, 1969.

A.D. Gosman, C. Lekakou, S. Politis, R.I. Issa, and M.K. Looney. Multidimensional modeling of turbulent two–phase flows in stirred vessels. *AIChE Journal*, 38:1946–1956, 1992.

X. Hu, A. Passalacqua, and R.O. Fox. Application of quadrature-based uncertainty quantification to the NETL small-scale challenge problem SSCP-I. *Powder Technology*, 272:100–112, 2015.

H.M. Hulburt and S. Katz. Some problems in particle technology: A statistical mechanical formulation. *Chemical Engineering Science*, 19:555–574, 1964.

M. Hussain, J. Kumar, and E. Tsotsas. Modeling aggregation kinetics of fluidized bed spray agglomeration for porous particles. *Powder Technology*, 270:584–591, 2015.

M. Jasińska, J. Bałdyga, S. Hall, and A.W. Pacek. Dispersion of oil droplets in rotor–stator mixers: Experimental investigations and modeling. *Chemical Engineering and Processing: Process Intensification*, 84:45–53, 2014.

M. Karimi, G. Akdogan, K.H. Dellimore, and S.M. Bradshaw. Comparison of different drag coefficient correlations in the cfd modelling of a laboratory-scale rushton-turbine flotation tank. In *The Ninth International Conference on CFD in the Minerals and Process Industries*, 2012.

S. Kumar and D. Ramkrishna. On the solution of population balance equations by discretization–I. A fixed pivot technique. *Chemical Engineering Science*, 51:1311–1332, 1996.

S. Kumar, V. Ganvir, C. Satyanand, R. Kumar, and K.S. Gandhi. Alternative mechanisms of drop breakup in stirred vessels. *Chemical Engineering Science*, 53:3269–3280, 1998.

M. Laakkonen, V. Alopaeus, and J. Aittamaa. Validation of bubble breakage, coalescence and mass transfer models for gas–liquid dispersion in agitated vessel. *Chemical Engineering Science*, 61:218–228, 2006.

G.L. Lane, M.P. Schwarz, and G.M. Evans. Numerical modelling of gas–liquid flow in stirred tanks. *Chemical Engineering Science*, 60:2203–2214, 2005.

Y. Liao and D. Lucas. A literature review of theoretical models for drop and bubble breakup in turbulent dispersions. *Chemical Engineering Science*, 64:3389–3406, 2009.

Y.L. Lin, K. Lee, and T. Matsoukas. Solution of the population balance equation using constant-number Monte Carlo. *Chemical Engineering Science*, 57:2241–2252, 2002.

H. Luo and H.F. Svendsen. Theoretical model for drop and bubble breakup in turbulent dispersions. *AIChE Journal*, 42:1225–1233, 1996.

J.Y. Luo, R.I. Issa, and A.D. Gosman. Prediction of impeller–induced flow in mixing vessels using multiple frames of reference. In *8th European Conf. on Mixing, Cambridge*, 1994.

S. Maaß and M. Kraume. Determination of breakage rates using single drop experiments. *Chemical Engineering Science*, 70:146–164, 2012.

S. Maaß, T. Rehm, and M. Kraume. Prediction of drop sizes for liquid–liquid systems in stirred slim reactors. Part II: Multi–stage impellers. *Chemical Engineering Journal*, 168:827–838, 2011.

S. Maaß, N. Paul, and M. Kraume. Influence of the dispersed phase fraction on experimental and predicted drop size distributions in breakage dominated stirred systems. *Chemical Engineering Science*, 76:140–153, 2012.

D.L. Marchisio and R.O. Fox. Solution of population balance equations using the direct quadrature method of moments. *Journal of Aerosol Science*, 36: 43–73, 2005.

D.L. Marchisio and R.O. Fox. *Computational models for polydisperse particulate and multiphase systems*. Cambridge University Press, 2013.

D.L. Marchisio, R.D. Vigil, and R.O. Fox. Quadrature method of moments for aggregation–breakage processes. *Journal of Colloid and Interface Science*, 258:322–334, 2003.

D.L. Marchisio, M. Soos, J. Sefcik, and M. Morbidelli. Role of turbulent shear rate distribution in aggregation and breakage processes. *AIChE Journal*, 52(1):158–173, 2006.

C. Martínez-Bazán, J.L. Montanes, and J.C. Lasheras. On the breakup of an air bubble injected into a fully developed turbulent flow. Part 1. Breakup frequency. *Journal of Fluid Mechanics*, 401:157–182, 1999.

E.D. McGrady and R.M. Ziff. Shattering transition in fragmentation. *Physical Review Letters*, 58(9):892–895, 1987.

R. McGraw. Description of aerosol dynamics by the quadrature method of moments. *Aerosol Science and Technology*, 27:255–265, 1997.

C. Meneveau and K.R. Sreenivasan. The multifractal nature of turbulent energy dissipation. *Journal of Fluid Mechanics*, 224:429–484, 1991.

G. Montante, K.C. Lee, A. Brucato, and M. Yianneskis. Numerical simulations of the dependency of flow pattern on impeller clearance in stirred vessels. *Chemical Engineering Science*, 56:3751–3770, 2001.

A. Passalacqua and R.O. Fox. Implementation of an iterative solution procedure for multi–fluid gas–particle flow models on unstructured grids. *Powder Technology*, 213:174–187, 2011.

E.L. Paul, V.A. Atiemo-Obeng, and S.M. Kresta. *Handbook of industrial mixing: Science and practice*. John Wiley & Sons, 2004.

M. Petitti, D.L. Marchisio, M. Vanni, G. Baldi, N. Mancini, and F. Podenzani. Effect of drag modeling on the prediction of critical regime transitions in agitated gas–liquid reactors with bubble size distribution modeling. *Multiphase Science and Technology*, 21:95–106, 2009.

M. Petitti, M. Vanni, D.L. Marchisio, A. Buffo, and F. Podenzani. Simulation of coalescence, break-up and mass transfer in a gas–liquid stirred tank with CQMOM. *Chemical Engineering Journal*, 228:1182–1194, 2013.

W. Podgórska. Scale–up effects in coalescing dispersions–Comparison of liquid–liquid systems differing in interface mobility. *Chemical Engineering Science*, 60:2115–2125, 2005.

W. Podgórska. *Drop breakup and coalescence in intermittent turbulent field.* Oficyna Wydawnicza Politechniki Warszawskiej, 2006a.

W. Podgórska. Modelling of high viscosity oil drop breakage process in intermittent turbulence. *Chemical Engineering Science*, 61:2986–2993, 2006b.

W. Podgórska and J. Bałdyga. Drop break-up and coalescence in a stirred tank. *Task Quarterly*, 7:409–424, 2003.

D. Ramkrishna. Drop-breakage in agitated liquid–liquid dispersions. *Chemical Engineering Science*, 29:987–992, 1974.

D. Ramkrishna. *Population balances: Theory and applications to particulate systems in engineering.* Academic press, 2000.

H. Rusche. *Computational fluid dynamics of dispersed two–phase flows at high phase fractions.* PhD thesis, Imperial College London, 2003.

L. Schiller and A. Naumann. A drag coefficient correlation. *VDI Zeitung*, 77:51–86, 1935.

C. Yuan and R.O. Fox. Conditional quadrature method of moments for kinetic equations. *Journal of Computational Physics*, 230:8216–8246, 2011.

W. Zhang and C. You. Numerical approach to predict particle breakage in dense flows by coupling multiphase particle–in–cell and Monte Carlo methods. *Powder Technology*, 283:128–136, 2015.